Experimental study on the flow structures and dynamics of turbulent Rayleigh-Bénard convection in an annular cell

Ji-Li Zheng [1] and Yu-Lu Liu [1,2,*]

[1] *Shanghai Institute of Applied Mathematics and Mechanics, School of Mechanics and Engineering Science, Shanghai University, Shanghai 200072, China*

[2] *School of Science, Shanghai Institute of Technology, Shanghai 201418, China*

(Received 1 April 2023; accepted 4 June 2023; published 29 June 2023)

We conduct an experimental study on the flow structures and dynamics of turbulent Rayleigh-Bénard convection in an annular cell with radius ratio $\eta \simeq 0.5$ and aspect ratio $\Gamma \simeq 4$. The working fluid is water with a Prandtl number of $\mathrm{Pr} \simeq 5.4$, and the Rayleigh number (Ra) ranges from 5.05×10^7 to 5.05×10^8. The multithermal-probe method and the particle image velocimetry technique are employed to measure the temperature profiles and the velocity fields, respectively. Two distinct states with multiroll standing waves are observed, which are the quadrupole state (QS) characterized by a four-roll structure and the sextupole state (SS) by a six-roll structure. The scaling exponents of Reynolds number Re with Ra are different for the two states, which are 0.56 for QS and 0.41 for SS. In addition, the standing waves become unstable upon tilting the cell by 1° in relation to the horizontal plane, and they evolve into traveling waves. At relatively high Ra, for instance, $\mathrm{Ra} \geqslant 2.55 \times 10^8$, it is observed that the traveling wave state SS undergoes a transition to the traveling wave state QS. However, the opposite transition from QS to SS is not observed in our experiments. Our findings provide insights into the flow structures and dynamics in the convection flow with rotation symmetry.

DOI: 10.1103/PhysRevE.107.065112

I. INTRODUCTION

Thermally driven convection is a ubiquitous phenomenon observed in natural, industrial, and domestic settings and has been extensively studied in various enclosed systems with diverse geometries [1]. A classical model for studying thermal convection is Rayleigh-Bénard convection (RBC) [2], which describes the fluid flow in an enclosed sample that is cooled from above and heated from below. This system is governed by two dimensionless parameters, namely, the Rayleigh number $\mathrm{Ra} = \alpha \Delta g H^3/(\nu\kappa)$ quantifying the strength of a buoyancy-driven force, and the Prandtl number $\mathrm{Pr} = \nu/k$, which is the ratio between momentum and thermal diffusion where Δ represents the temperature difference between the top and bottom plates; H is the height of the fluid layer; α, κ, and ν are the thermal expansion coefficient, thermal diffusivity, and kinematic viscosity of the fluid, respectively, and g denotes the gravitational acceleration. Another important control parameter relates to the geometry of the convection cell, which is the aspect ratio $\Gamma = D/H$, where D is the cell diameter. The response parameters typically of interest are the Nusselt number $\mathrm{Nu} = JH/(\chi\Delta)$, and the Reynolds number $\mathrm{Re} = UH/\nu$, which represent the dimensionless heat transport efficiency and flow strength, respectively. Here J is the average heat flux, χ is the thermal conductivity of the convective fluid, and U is the typical averaged (spatial and temporal) velocity.

Studies of RBC have focused on the transport properties, such as heat and momentum, represented by Nu and Re, respectively. One major challenge is how to overcome the transport bottleneck caused by the boundary layer [3]. To tackle this issue, numerous efforts have been undertaken, including modifying the boundaries with rough elements [4–6] and injecting gas bubbles at the boundaries [7]. Manipulating coherent structures is also a tempting strategy to control turbulent transport in thermal turbulence [8], which can be achieved through various approaches including geometrical confinement [9–11], additional forces [12–15], polymer additives [16,17], and convection modulation [18–20].

Using the annular geometry is a kind of effective approach to manipulate coherent structures in thermal convection, leading to changes in transport properties [21]. The flow pattern and the formation of coherent structures are affected by the geometry of the annular space, which includes Γ and the radius ratio $\eta = R_i/R_o$ (where R_i and R_o are the inner and outer radii of the convection cell). This convection system has gained considerable attention due to its relevance to both natural and engineering applications, for example, the convection inside the Earth, polymerase chain reaction in annular cells, cooling of nuclear reactors, and crystal preparation using the pulling method [22–26]. The significance of studying the annular convection system is also due to its geometrical similarity to the twin model, the turbulent Taylor-Couette system [27,28]. Previous research on RBC in annular geometries mainly focused on flow instabilities and pattern evolution, particularly in the laminar regime or the onset of convection [29–31]. Recently, the RBC in annular cells with varying aspect ratios was investigated by Zhu *et al.* [32,33]. It was found that Γ

*Corresponding author: ylliu@shu.edu.cn

does not significantly affect heat transport or the statistical properties of local temperature, but it does have an impact on the flow dynamics. In addition, the effects of radius ratio η was systematically studied by Wang *et al.* [34] in the annular centrifugal RBC system. The results indicated that larger η resulted in a weaker zonal flow intensity but higher efficiency of heat transport, whereas decreasing η caused greater deviation of bulk temperature from the arithmetic mean due to curvature effects and radially dependent centrifugal forces. Despite the previous studies, the dynamics and finer-grained structures of turbulent RBC in annular geometries have not been comprehensively studied.

In turbulent RBC, the existence of multiple states characterized by distinct large-scale structures or statistical properties has generated significant interest. Various multiroll structures and flow-mode transitions were observed in many experimental studies, with the cell geometry not restricted to the annular one [21,35–38]. The emergence of different turbulent states, even for identical control parameters, is determined by the initial conditions and the Γ, with the transport properties being dependent on the realized state [39]. The flow states with more horizontal rolls enhance heat transport efficiencies for $\Gamma > 1$ [37,39]. In contrast, more convection rolls that are stacked on top of each other in slender containers with $\Gamma \leqslant 1$ lead to weaker heat and momentum transport [37,40]. Furthermore, the transition of turbulent states is attributed to flow instability, which causes spontaneous symmetry breaking [21,40].

In addition to the spatial behavior of multiple states, there is also an intriguing temporal phenomenon: The transition from an axisymmetric steady state, known as standing waves, to azimuthal traveling waves [41]. This transition is triggered by a complex eigenvalue corresponding to a nonaxisymmetric eigenvector, leading to a Hopf bifurcation and resulting in standing and traveling waves with different symmetries [42]. The standing waves exhibit reflection symmetry in θ with respect to a specific angle θ_0, while the traveling waves break this symmetry. An intriguing experimental study on this phenomenon was conducted by Hof, Lucas, and Mullin [43]. They observed several distinct stable patterns for the same final Ra and also reported a transition from a state of axisymmetric stability to the emergence of azimuthal waves. A similar traveling-wave convection was observed in an annular container with a large aspect ratio (the ratio of height to radial width to mean circumference is 1:1.63:105.3) [44], where the convection rolls align themselves radially and propagate azimuthally. There was a competition between several nonequilibrium states, resulting in an abundant variety of dynamical behavior, such as coexisting regions of conduction and convection, sources and sinks of convection rolls, and more complex spatiotemporal defects.

This paper presents an experimental investigation on flow structures and dynamics of RBC in an annular cell with $\Gamma = 4$. The current work aims to investigate the following issues: (1) the occurrence of multiple states and mode transitions in the annular system with weak horizontal constraints ($\eta \simeq 0.5$); (2) the spatial structures and momentum transport properties for distinct turbulent states; and (3) the existence of azimuthal traveling-wave motion caused by broken spatial symmetry. To address these issues, two kinds of measurements were utilized. First, a multithermal-probe method [21] was employed to measure the temperature profile and flow strength at the midheight of the fluid layer. Second, the planar particle image velocimetry (PIV) technique [45] was used to measure the two-dimensional (2D) velocity maps in different cross sections of the cell [46–48]. The remainder is organized as follows. We describe the experimental setup and methods in Sec. II. The results will be presented and discussed in Sec. III, which consists of two subsections. In Sec. III A, the time-averaged flow structures are displayed and the scaling of Re dependence on Ra is also discussed. Section III B introduces the spatiotemporal characteristics of the traveling waves. Finally, the findings are summarized in Sec. IV.

II. EXPERIMENTAL APPARATUS AND METHODS

A. Experimental setup

The experiment is conducted in an annular convection cell, as illustrated in Fig. 1(a), mainly including upper and lower plates, an upright inner cylinder, and an outer cylinder with a square jacket. The cylinders and jacket are made of transparent plexiglass, which allows for better optical observation while ensuring thermal insulation of the side walls. The height of both cylinders is $H = 10$ cm. The inner cylinder has a wall thickness of 3.6 mm and an outer diameter of $D_i = 20$ cm, while the outer cylinder has a wall thickness of 5.6 mm and an inner diameter of $D_o = 39$ cm. Thus, the aspect ratio is $\Gamma = D_o/H \simeq 4$ and the radius ratio is $\eta = D_i/D_o \simeq 0.5$. The square jacket is slightly wider than the cell, hence covering its entire circumference, but it does not cover the entire cell height. An upper corner of the jacket features a water injection port with a diameter of 1 cm. During the experiment, the jacket is filled with pure water to reduce the influence of the curved wall on the PIV optical path. The annular plates, made of copper, have inner and outer diameters of 15 cm and 45 cm, respectively. The upper plate is cooled with a thermal bath (Polyscience AD15R-40-A12Y) with a temperature stability of 0.01 K. Conversely, the lower plate is heated by four identical fan-shaped Kapton film heaters (with an inner diameter of 20 cm and an outer diameter of 40 cm) connected in parallel to a direct-current (DC) power supply (SGI 330X15D) with 99.99% long-term stability.

It should be noted that the heating method would unavoidably result in a minor experimental imperfection, i.e., the slight nonuniformity in the heating of the bottom plate. Specifically, the heat provided by the DC power could be more concentrated in the center region of certain fan-shaped heaters, which acts as a local "small thermal disturbance" [49], leading to the intermittent burst of hot plumes in the heat-concentrated region. The temperatures of each conducting plate are measured by eight thermistors (model 44032, Omega) with a diameter of 2 mm. Other details regarding the cell can be learned from Ref. [32].

B. Multithermal-probe and PIV measurements

As shown in Fig. 1, the Cartesian coordinate for experiments is defined such that their origin coincides with the center of the lower plate surface and the z axis points upward.

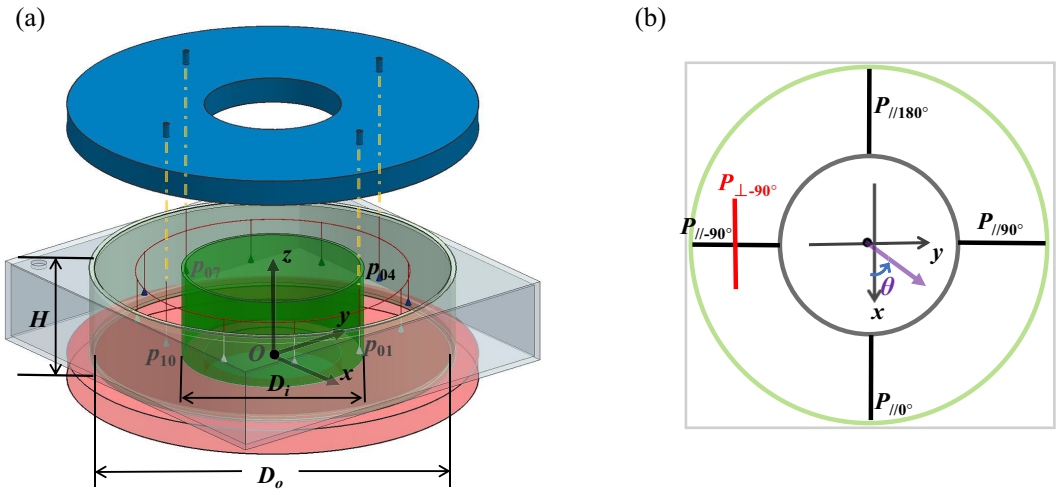

FIG. 1. Schematic diagram of (a) the annular convection cell and (b) the top view of PIV planes. Twelve temperature probes (p_{01}, $p_{02}, \ldots, p_{12}$) are employed to monitor the time series of temperature along the circumference between the inner and outer cylinders, at the mid-height of the cell. The phase angle of the annular circumference is determined by taking the positive direction as 0 degrees along the x axis and the counterclockwise direction as positive. The PIV measurement planes are oriented parallel to the vertical axial planes of $Oxyz$, i.e., perpendicular to the conducting plates. Four radially distributed black planes along the circumference are labeled as $P_{//-90°}$, $P_{//0°}$, $P_{//90°}$, and $P_{//180°}$ according to their phase angles, and the chordal red planes that perpendicularly bisect the radial planes are represented as $P_{\perp 0°}$. Probe p_{01} is located in the center of $P_{//0°}$ and so on.

The x axis and y axis of the coordinate $Oxyz$ point to the front and right, respectively.

To visually reveal the multiroll structure and monitor its azimuthal motion more effectively, the multithermal-probe method [21] is employed to measure the temperature of the convective fluid. Since the temperature of the hot (cold) thermal plume is higher (lower) than the horizontal average, the flow structure and dynamics can be reflected by the temperature profile. As shown in Fig. 1(a), 12 small thermistors (GAG22K7MCD419, Measurement Specialties) with a diameter of 400 μm are fixed on a wire frame and inserted uniformly along the circumference between the inner and outer cylinders, at the half height of the fluid layer. They are labeled counterclockwise from p_{01} to p_{12}, where p_{10} is located near the center of planes $P_{//-90°}$ and $P_{\perp-90°}$. The resistance values of 12 small thermistors in fluid as well as 16 large thermistors in plates are recorded by a digital multimeter (KEYSIGHT 34972A) at a sampling frequency of 2.5 Hz and are converted into corresponding temperatures through calibrated coefficients. At each time step, the temperature profile is expanded using discrete Fourier series, i.e.,

$$T(i) = T_0 + \sum_{n=1}^{6} A_k \cos[(\pi/6)i + \theta_k], \quad (i = 1 \ldots 12), \quad (1)$$

where A_k and θ_k are, respectively, the amplitude and the phase of the kth Fourier mode and T_0 is the azimuthally averaged temperature. The flow state is identified by the predominant Fourier mode corresponding to the largest $A_k(t)$.

Velocity fields are measured using the PIV method with a system consisting of a 532-nm laser (MGL-F-532-3W), a high-speed camera (Phantom V341) with 12-bit dynamic range and 2560 × 1600-pixel spatial resolution, and a signal generator (Owon, AG1012) which reduced the camera's sampling frequency to below 10 Hz. The PIV planes at which the velocity field was measured are illustrated in Fig. 1(b), and all are located at or parallel to the vertical axis. To ensure a straight optical path from the shooting plane to the camera, we always align the four vertical planes of the jacket with the horizontal axis when assembling the outer cylinder. Polyamide spheres with a 20-μm diameter (density 1.03 g/cm^3) are chosen as seed particles. The camera's spatial resolution is set to 1024 × 1024. The square area captured by the camera does not include the upper and lower boundary layers, as strong reflections in the boundary layer would interfere with the measurement. A subwindow of 32 × 32 pixels is used with 50% overlap to calculate each 2D velocity vector, resulting in a spatial resolution of 1.51 mm. The camera adopts a dual-frame capture method, and the time interval between each image pair is 50 000 μs to ensure that particle movements are within an appropriate range relative to the inquiry window [45].

For the standing waves, each measurement lasts for 1 hour with a sampling frequency of 2.5 Hz, resulting in more than 9000 instantaneous fields and over 18 000 particle images for the three focus Ra values of $\mathrm{Ra_{min}} \simeq 5.05 \times 10^7$, $\mathrm{Ra_{med}} \simeq 2.55 \times 10^8$, and $\mathrm{Ra_{max}} \simeq 5.05 \times 10^8$. For the investigation of traveling wave motion, plane $P_{\perp-90°}$ is monitored for up to 12 hours with a reduced sampling frequency of 0.2 Hz, while the other settings remain unchanged. In this way, each group of measurements yields over 8640 instantaneous velocity vector fields. The velocity components along x, y, and z are denoted by u, v, and w, respectively, and the corresponding time-averaged quantities are U, V, and W.

C. Experimental conditions

The working fluid used is degassed water at a mean temperature of 30° C, leading to a Prandtl number of Pr = 5.4. The Rayleigh number range is achieved by varying the temperature difference Δ across the fluid layer between 2.0° C

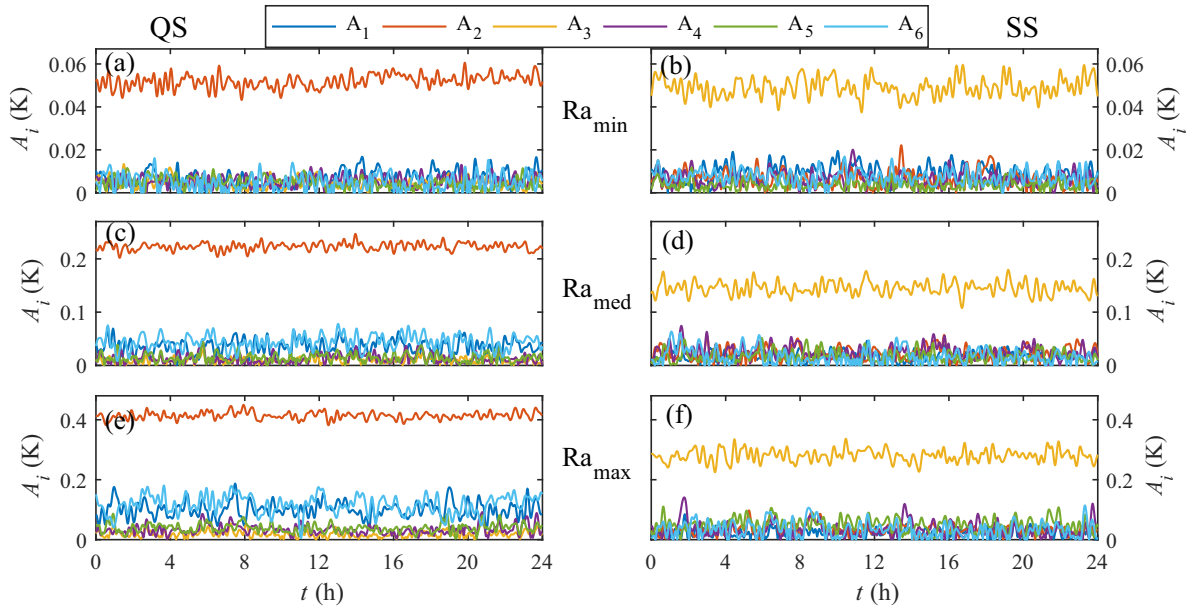

FIG. 2. Time series of the amplitude of the first six Fourier modes for the temperature profile under QS (left) and SS (right) at different Ra. (a, b), (c, d), and (e, f) correspond the results for $\mathrm{Ra_{min}} = 5.05 \times 10^7$, $\mathrm{Ra_{med}} = 2.55 \times 10^8$, and $\mathrm{Ra_{max}} = 5.05 \times 10^8$, respectively.

and 20° C, resulting in $5.05 \times 10^7 \leqslant \mathrm{Ra} \leqslant 5.05 \times 10^8$. In this scalar turbulence, the scalar diffusivity is smaller than the viscous diffusivity and the smallest scale in the problem is the Batchelor scale [50]. To prevent temperature drift and to reduce heat exchange between the convection cell and the surrounding environment, we use an air conditioner to keep the laboratory at around 30° C. Throughout the course of the experiment, a constant power is applied to the bottom plate of the cell to maintain a constant-flux boundary condition. Despite this heating, the temperature of the bottom plate remains effectively constant at steady state. On the other hand, the temperature of the top plate is controlled to maintain a constant-temperature boundary condition.

III. RESULTS AND DISCUSSION

A. Standing waves

In our experiments, thermal plumes are typically generated in certain regions when the annular cell is horizontal, as a result of a "small disturbance" caused by the slightly nonuniform heating of the bottom plate. Each pair of hot and cold plumes drives a roll that maintains a stable self-rotation around its core, forming a standing wave convection [41]. Interestingly, depending on the initial $\mathrm{Ra_0}$, two standing wave states with different azimuthal wave numbers are observed, which is consistent with the statement by Wang *et al.* [39] that "what state the system takes depends on the initial conditions". The realized two states are termed the quadrupole state (QS) and sextupole state (SS), respectively. Specifically, when the DC power supply and thermal bath are started with larger power, resulting in $\mathrm{Ra_0} = \mathrm{Ra_{med}}$ after the convection is stable (generally after 7 hours), a four-roll structure (QS) will form in the flow field. This QS state remains unchanged when the Ra varies between $\mathrm{Ra_{min}}$ and $\mathrm{Ra_{max}}$ during subsequent experiments after the state is established. In contrast, when the DC power supply and thermal bath are started with smaller power, resulting in $\mathrm{Ra_0} = \mathrm{Ra_{min}}$ after the convection is stable (usually after 3 hours), a six-roll structure (SS) will form in the flow field. This SS state remains unchanged within the measured Ra range. Therefore, different initial $\mathrm{Ra_0}$ lead to the appearance of different standing wave convection states QS and SS, which stably exist in the annular RBC system once the convection is stable.

We show first in Fig. 2 the amplitudes of all the first six Fourier modes of the temperature profiles at three different Ra values. To eliminate temperature fluctuation spikes caused by the plumes and retain the primary features of the original data, Fourier transforms were applied to the temperature time series measured at each space point to perform low-pass filtering. The left three panels [Figs. 2(a), 2(c), and 2(e)] show that the amplitude of the second mode (red) is significantly larger than that of other modes, indicating that the second mode dominates, corresponding to the QS convection state. The right three panels [Figs. 2(b), 2(d), and 2(f)] show that the third Fourier mode dominates, corresponding to the SS state. Furthermore, the dominant mode will not transition from one to the other with the evolving of time. Therefore, QS and SS are indeed two clearly distinguishable turbulent states, and the states are maintained in the standing wave convection.

Then the time-averaged azimuthal temperature profiles at the midheight of the fluid layer for the two identified flow structures are shown in Figs. 3(a) and 3(b). Based on the distribution of the temperature profiles, schematic diagrams of the corresponding flow structures for QS and SS are drawn in Figs. 3(c) and 3(d), respectively. It can be seen that there is usually a temperature peak caused by the hot plumes near the location of probe p_{10}, which is due to the existence of a small yet noticeable thermal disturbance at the azimuth of approximately −90°. The hot ascending and cold descending regions of the large-scale flow (LSF) appear alternatively along the azimuthal direction. Specifically, a separation of $\pi/2$ between

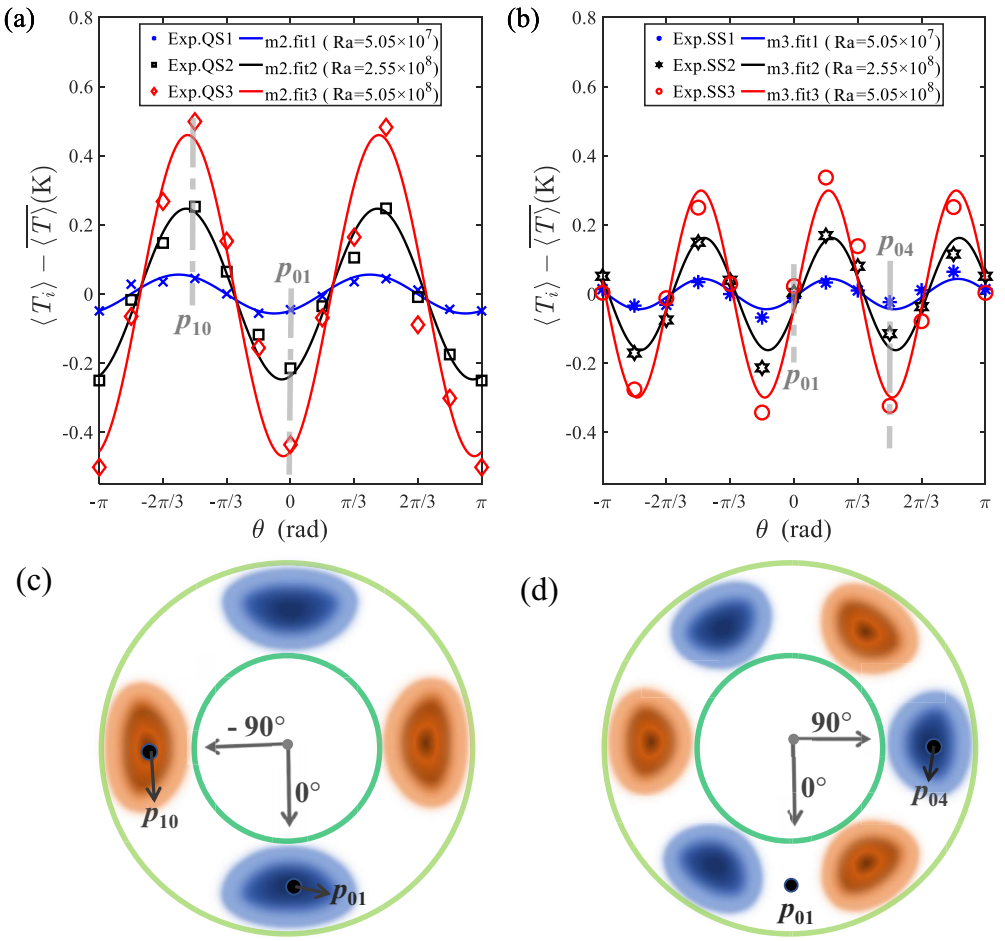

FIG. 3. Mean temperature profiles measured from the midheight of the convective fluid by the 12 temperature probes, at the moment when (a) the second mode or (b) the third mode is dominant, respectively. Experimental data denoted by markers are fitted by using lines calculated based on the second (for QS) and third (for SS) Fourier modes. The marks and lines in blue, black, and red correspond to three different Ra numbers: $\mathrm{Ra_{min}} = 5.05 \times 10^7$, $\mathrm{Ra_{med}} = 2.55 \times 10^8$, and $\mathrm{Ra_{max}} = 5.05 \times 10^8$. $\langle T_i \rangle$ denotes the time-averaged temperature for the ith thermistor and $\overline{\langle T \rangle}$ denotes the average temperature for all the thermistors over all times. The flow schematic diagram show the midheight cut of the flow for (c) QS and (d) SS, viewed from above. The red patterns represent up-flow and the blue patterns represent down-flow.

the hot and cold plumes corresponds to QS, while a separation of $\pi/3$ corresponds to SS. In addition, the azimuthal phase of the temperature curve has little deviation at different Ra, but the amplitude changes significantly. For the same Ra, SS with more convection rolls exhibits lower temperature amplitude than QS. The results show that once the convection state of the standing wave is established, any mode transition (from QS to SS or vice versa) similar to that reported by Xie *et al.* [21] is not observed in our system, as the Ra number increases within the measurement range. It should be emphasized that the cell used by Xie *et al.* exhibits significant geometric differences from ours, especially in terms of radius ratio, where $\eta = 0.88$, leading to more stringent horizontal geometric constraints.

Figure 4 shows the velocity vector maps of QS (left) and SS (right) obtained from PIV measurements in four radial cross sections at $\mathrm{Ra_{med}}$. For QS, the main falling flow is present in planes $P_{//180^\circ}$ [Fig. 4(a)] and $P_{//0^\circ}$ [Fig. 4(b)], separated by π azimuth, while the rising arises in the other two oppositely oriented planes $P_{//-90^\circ}$ [Fig. 4(c)] and $P_{//90^\circ}$ [Fig. 4(d)]. As for SS, $P_{//180^\circ}$ [Fig. 4(e)] and $P_{//0^\circ}$ [Fig. 4(f)] cut through the center of the rolls and exhibit very small mean velocity in this region. Conversely, the vertical upward and downward main flows are observed in planes $P_{//-90^\circ}$ [Fig. 4(g)] and $P_{//90^\circ}$ [Fig. 4(h)], located in the hot and cold plume regions, respectively.

Note that there are some differences in the local flow fields near the inner and outer cylinders. As shown in Figs. 4(a) to 4(d) and 4(g) and 4(h), a relatively large corner vorticity exists near the inner wall, preventing the upwelling or downwelling flows along the inner wall from directly impinging on the opposite plate. However, the typical large-scale circulation (LSC) does not form in these planes, and the regions corresponding to the peaks and valleys in the temperature profiles are primarily characterized by upwelling and downwelling motions, respectively, which dominate the main flow. The velocity results confirm the LSF structures revealed by the temperature profiles shown in Fig. 3.

To investigate the dependence of momentum transport on the Ra, PIV measurements were conducted in planes $P_{//-90^\circ}$ and $P_{\perp-90^\circ}$, where significant vertical velocities were present. The momentum transport is characterized by the Re, which is defined based on the maximum vertical velocity $W_{\max}$ in the

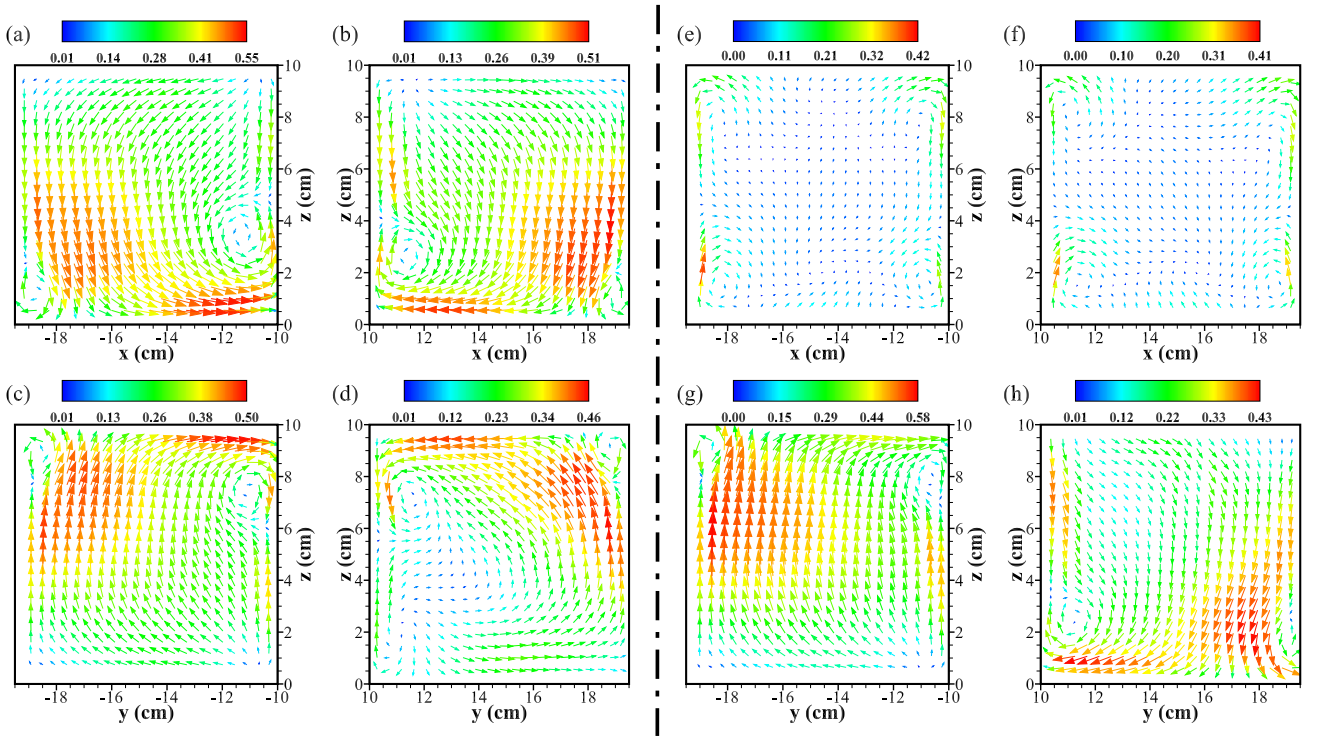

FIG. 4. Coarse-grained vector maps of the mean velocity field corresponding to QS (left) and SS (right) for $\mathrm{Ra_{med}} = 2.55 \times 10^8$ measured in four radial planes: (a, e) $P_{//180^\circ}$; (b, f) $P_{//0^\circ}$; (c, g) $P_{//-90^\circ}$; and (d, h) $P_{//90^\circ}$. The velocity magnitude V_{mag} calculated by $(U^2+W^2)^{1/2}$, $(V^2+W^2)^{1/2}$ is coded in both color and the length of the arrows in units of cm/s. For clarity, the vector arrows are displayed at intervals of three.

time-averaged 2D field

$$\mathrm{Re} = \frac{W_{\max} H}{\nu}. \tag{2}$$

Figure 5 shows how Re depends on Ra. We observe that for both QS (hollow markers) and SS (solid markers), the Re values measured in $P_{//-90^\circ}$ and $P_{\perp-90^\circ}$ at the same Ra are close, and the exponents of the fitted scaling law are also approximate. However, we note that the scaling laws differ for the two distinct flow states. Specifically, in the lower Ra range, the Re for QS is significantly lower than that for SS. As Ra increases, the Re for QS gradually approaches that for SS. As a consequence, QS exhibits a larger scaling exponent reaching 0.56, which is significantly higher than that for SS which is 0.41. Notably, the scaling exponent of 0.56 is consistent with previous findings. Lam *et al.* [51] reported the experimental local exponents between 0.50 and 0.68 for the $\mathrm{Re}_{U,\max}$ (maximum-velocity-based Re) as Pr increases from 3 to 1200, and Chen *et al.* [52] obtained a PIV result of 0.55 for $\mathrm{Pr} = 4$–7, with their Re defined through the typical velocity of the LSC.

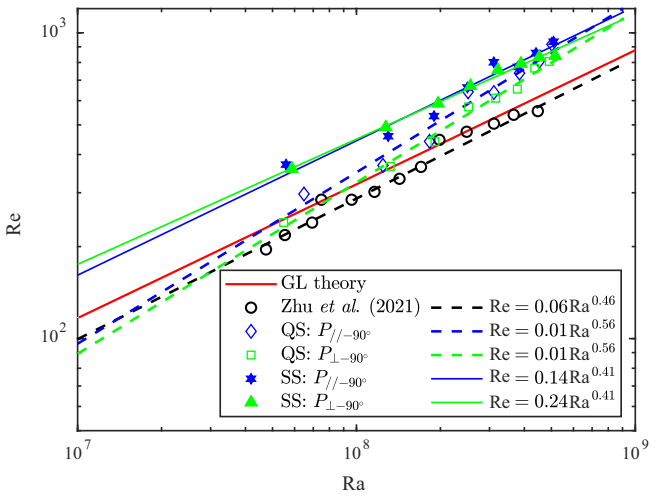

FIG. 5. Measured Re as a function of Ra. Results in planes $P_{//-90^\circ}$ and $P_{\perp-90^\circ}$ are coded in blue and green, respectively. Hollow diamonds and squares fitted with dashed lines correspond to QS, while solid hexagonal stars and triangles fitted with solid lines correspond to SS.

Additionally, our results were compared with experimental data from Zhu *et al.* [33], who determined the scaling exponent of Re with Ra to be 0.46 for the same four-roll state in a similar cell. Their Re was calculated based on the shedding frequency of plumes, denoted as Re_f, which typically results in a lower Re value and scaling exponent than calculating it using the typical velocity of the LSF, denoted as Re_U [46,53]. Our data for QS shown in Fig. 5 are consistent with this trend and thus reasonably larger than the results of GL theory and Zhu's experiment. However, the scaling exponent of 0.41 for SS in our study is smaller than all previously reported values, including the 0.46 from Zhu *et al.* Thus, alterations in the Ra affect low-order modes more profoundly than high-order modes. When the number of rolls occupying the cell space increases from four to six, the ascending flow is straightened more by the rolls on both sides, resulting in an increase in

the vertical velocity component, particularly at low Ra. The difference in scaling laws between the two states is related to the difference in roll morphology, which is a flattened elliptical for QS and closer to a circle for SS.

B. Traveling waves

During the experiments for the horizontal convection cell, the standing waves are locked within limited spatial phase due to "small thermal disturbances" and the traveling waves are not observed. Theoretically, the traveling waves might exist in the idealized system as in the works of Borońska and Tuckerman [41] as well as Brown and Ahleras [54]. Thus, whether azimuthal traveling waves would generate in this annular turbulent RBC system needs to be further explored. To break the azimuthal symmetry, the cell is tilted far away from the plumes by 1° relative to the central vertical axis, so that an intriguing phenomenon of traveling waves [41] occurs: All rolls not only rotate about their cores but also propagate around the circumference of the cell, which is similar to the rotation and revolution of the planets. The phenomenon discussed here resembles the experimental findings of Kolodner *et al.* [44], who also observed similar behavior in an annular cell, albeit with a binary fluid mixture as the convective medium. However, tilting the cell along the orientations of the hot plumes induced by the "small thermal disturbances" in a horizontal cell tend to further lock the LSF.

We employ multithermal probes to track the motion of plumes and rolls. The temperature profiles at three different moments in time are shown in Fig. 6. The results demonstrate a pronounced time-dependent phase variation that increases gradually and may exceed 2π. This behavior contradicts the typical characteristics of standing waves, which usually exhibit a plume swinging with equal probability to the left and right [33], and consequently, the phase change of the temperature profile remains within a limited range. Furthermore, our experiments show that SS moves slower than QS for the same Ra. Although the filtered temperature profile exhibits a smaller amplitude compared to the actual measurement data [refer to Figs. 3(a) and 3(b)], the exact amplitude magnitude is not critical for our conclusions. Based on the observed temperature profiles, the flows associated with two traveling wave states, QS and SS, were inferred. The originally symmetric flows become unstable along the azimuthal directions due to the presence of angular flows. Figures 6(c) and 6(d) show the schematic diagrams of the upward (or downward) flows. The flows at this situation represent counterclockwise traveling waves as the spatial phase of the temperature profile continuously increases with time.

During traveling wave motion, not only temperature, but also velocity fields exhibit periodic changes. Therefore, while measuring the temperature profile, PIV measurements lasting 12 hours were performed in $P_{\perp-90^\circ}$ to obtain velocity information. Figure 7 shows the time series of temperature- and velocity-dependent quantities for QS (left) and SS (right) at $\mathrm{Ra_{med}}$. The second- and third-order Fourier mode amplitudes, shown in both Figs. 7(a) and 7(g), serve to discern the dominant mode. In fact, the amplitudes of modes other than the second or third are negligible for the traveling waves, resembling the situation for standing waves, and are not shown here

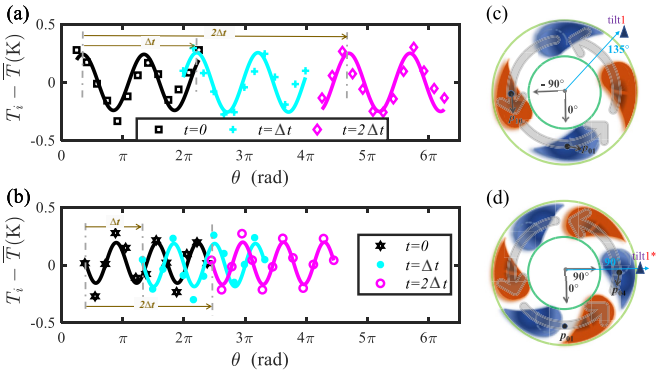

FIG. 6. Fourier-filtered instantaneous azimuthal temperature profile for $\mathrm{Ra_{med}} = 2.55 \times 10^8$ measured from the midheight of the convective fluid, at the moment when (a) the second mode or (b) the third mode is dominant, respectively. T_i denotes the instantaneous temperature for the ith thermistor and $\overline{T}$ denotes the average instantaneous temperature for all the thermistors. The filtered experimental data denoted by markers are fitted using lines calculated based on the second (for QS) and third (for SS) Fourier modes. The marks and lines in black, cyan, and magenta correspond to three different instants $t = 0$, $t = \Delta t$, and $t = 2\Delta t$ at intervals $\Delta t = 3$ h. The flow schematic diagrams show the midheight cut of the traveling waves for (c) QS and (d) SS, viewed from above. The red patterns represent up-flow and the blue represent down-flow. The circular arrows represent that the convection waves travel counterclockwise. The small triangle in the upper right corner indicates that the cell is elevated 1° (relative to the horizontal plane) along the 135° azimuth ("tilt1") for QS and 90° azimuth ("tilt1*") for SS.

for brevity. We observe that in Fig. 7(a), the amplitude of the second-order mode is significantly larger than that of the third order during the entire measurement time, indicating that the second-order mode is dominant and the corresponding flow state is QS. Conversely, in Fig. 7(e), the third-order mode dominates, and the corresponding flow state is SS. The azimuth phases as shown in Figs. 7(b) and 7(f) indicate that there exists a noteworthy contrast in the variation of the azimuthal angle over time for the two flow states QS and SS. Throughout the 12 hours, QS experienced an angular displacement of more than 25 rad, while SS experienced less than 12.3 rad, indicating that the mean angular travel speed of SS is no more than 1/2 of that of QS. Figures 7(c) and 7(g) display the angular speed Ψ of the propagating wave, which is computed using the expression

$$\Psi = \frac{d\theta}{dt} = \frac{\theta(t+\tau) - \theta(t)}{\tau}. \tag{3}$$

Here, θ represents the azimuth angle of the wave traveling in the angular direction and τ refers to the time interval of each azimuth. The angular speed fluctuates around the time-averaged value [5.75×10^{-4} rad/s for QS and 2.85×10^{-4} rad/s for SS], as denoted by the green dashed line, and the fluctuation range spans approximately one order of magnitude. Occasionally, the angular speed even becomes negative, indicating that the phases of the waves do not strictly increase or decrease monotonically with time. This observation suggests that the angular motion of traveling waves is an unstable process and sometimes exhibits oscillations back and forth

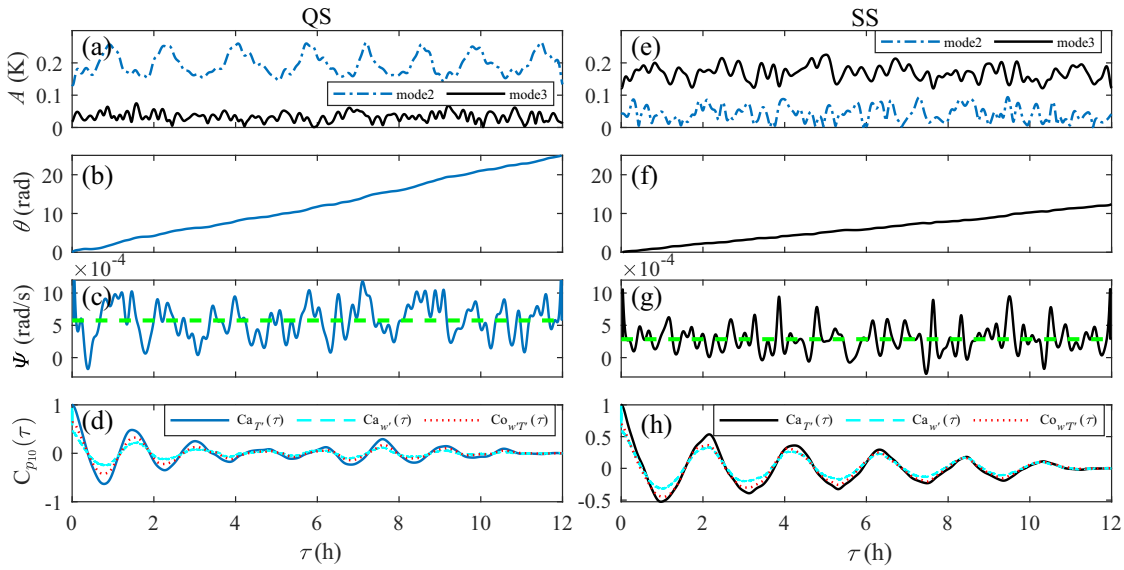

FIG. 7. The time series of data related to temperature and velocity for QS (left) and SS (right) during traveling wave motion for $\mathrm{Ra_{med}} = 2.55 \times 10^8$. The raised direction of the cell is along 135° azimuth for QS and 90° azimuth for SS. The time series of the second- and third-order Fourier mode amplitudes and phases are shown in (a, e), and (b, f), respectively. (c) and (g) correspond to the angular speed of traveling waves whose time-mean values are indicated by the green dashed lines. (d) and (h) display the autocorrelation $\mathrm{Ca}_{T'}(\tau)$ and $\mathrm{Ca}_{w'}(\tau)$ of temperature fluctuations T' (solid line) and vertical velocity fluctuations w' (dashed cyan line), as well as the cross-correlation $\mathrm{Co}_{w'T'}(\tau)$ between w' and T'(dotted red line) at point p_{10} (located near the center of $P_{\perp -90^\circ}$) as a function of delay time τ. The calculation expressions of the above correlation functions are as follows: $\mathrm{Ca}_{T'}(\tau) = \langle T'(t+\tau)T'(t)\rangle/\sigma(T')^2$; $\mathrm{Ca}_{w'}(\tau) = \langle w'(t+\tau)w'(t)\rangle/\sigma(w')^2$; $\mathrm{Co}_{w'T'}(\tau) = \langle w'(t+\tau)T'(t)\rangle/\sigma(w')\sigma(T')$. Here $\sigma(T')$ [$\sigma(w')$] is the root-mean-square value of T' [w'].

in their phase space. However, in general, the angular phase increases over time.

The correlation function provides a direct representation of the periodic variations in temperature and velocity fields. Thus, we conducted a sequential assessment of these correlation functions. Specifically, we present the autocorrelation function for temperature fluctuations T' and vertical velocity fluctuations w' at point p_{10}, which is situated near the center of $P_{//-90^\circ}$, as well as the cross correlation between w' and T' in Figs. 7(d) and 7(h). Our analysis of the autocorrelation function of T' and w', along with the cross-correlation function between the two, reveals an agreement between the two measurement methods of the multithermal probe and PIV. All correlation functions exhibit periodic variations, with a period of approximately 1.5 hours for the QS and 2.1 hours for the SS. The time for the two flow states to complete one revolution around the annular cell is calculated to be $1.5 \times 4/2 = 3$ hours for QS and $2.1 \times 6/2 = 6.3$ hours for SS, which is consistent with the results obtained by calculating the angular speed [$2\pi/(5.75 \times 10^{-4})/3600 = 3.04$ h for QS and $2\pi/(2.85 \times 10^{-4})/3600 = 6.12$ h for SS].

To explore the effects of Ra and the cell tilting on the traveling wave motion of the QS, temperature profiles were monitored at three different Ra numbers and two opposite tilt directions of the cell for up to 48 hours. Similarly, the amplitude and phase of the second Fourier mode that always dominates are presented in Fig. 8. The results demonstrate that an increase in Ra leads to higher amplitudes and larger azimuthal shifts, as shown in Fig. 8. At $\mathrm{Ra_{min}}$, the increment of θ within 48 hours is approximately 5 rad, which occurs when the LSF moves from an unstable to a stable position. In contrast, at $\mathrm{Ra_{med}}$ and $\mathrm{Ra_{max}}$, the net angular increments are approximately 70 rad and 100 rad, respectively. Furthermore, opposite tilt directions of the cell result in different turns of the traveling wave motion, which is manifested as positive and negative phase values. As an illustration, hot plumes in QS appear near the planes $P_{//-90^\circ}$ and $P_{//90^\circ}$ when the convection cell is horizontal. Upon raising the platform's pillar located in the azimuth of 135° by approximately 1°, the four rolls rotate counterclockwise around the z axis while also rotating themselves. Conversely, elevating the opposite pillar in the −45° azimuth causes the rolls to rotate clockwise around the z axis. At the same $\mathrm{Ra_{max}}$, the amplitudes are similar for both the clockwise and counterclockwise cases and the angular deviation remains close for a prolonged period. In addition, the overall propagation direction of traveling waves behaves unidirectionally over extended periods, which contrasts with the Brownian-like angular motion of the LSC in leveled cylindrical cells [35]. Interestingly, the motion of vortices in rotating turbulent convection can be accurately described within the framework of Brownian motion, as they exhibit ballistic and diffusive behaviors similar to inertial Brownian particles [55].

The observations of Fig. 8 suggest a complex relationship between the orientation of the cell tilting and the burst regions of plumes. When the cell is tilted along different azimuths, counterclockwise or clockwise traveling waves will occur, which is due to the combined effect of "small thermal disturbances" and cell tilting. First, the asymmetrical distribution of "disturbances" causes hot plumes to burst in asymmetrical preferential locations, leading to an asymmetrical spatial distribution and nonuniform flow intensity of convection rolls driven by plume pairs. As reported by Guo *et al.* [56], LSC

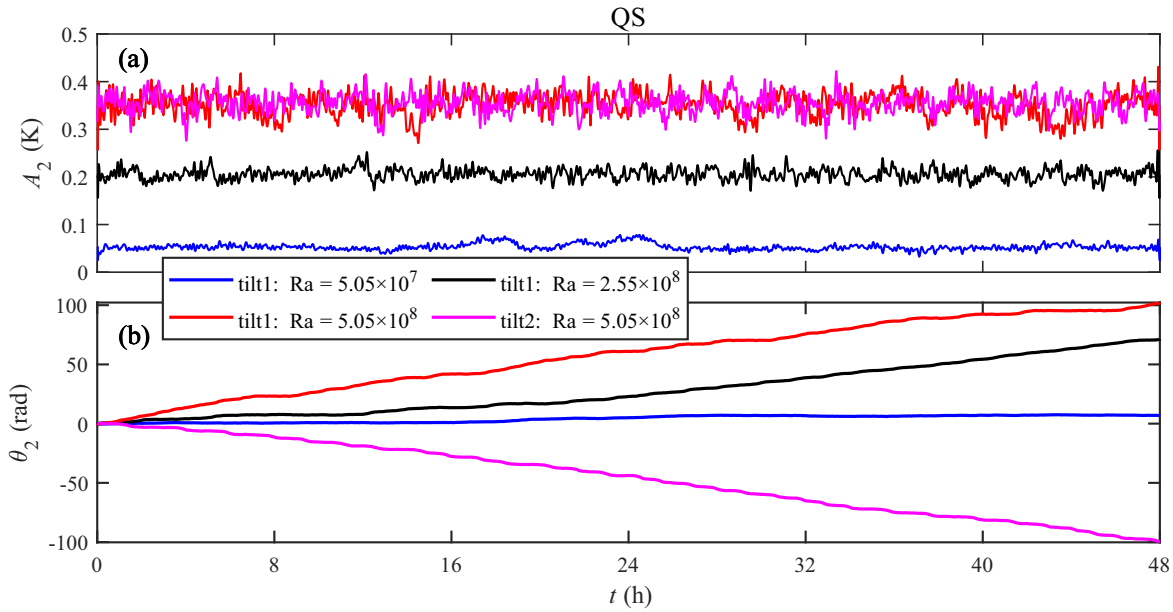

FIG. 8. The time series of the second-order Fourier mode (a) amplitude and (b) phase for QS at different Ra and cell tilting. The blue, black, and red lines represent the results for $\mathrm{Ra_{min}} = 5.05 \times 10^7$, $\mathrm{Ra_{med}} = 2.55 \times 10^8$, and $\mathrm{Ra_{max}} = 5.05 \times 10^8$, respectively. Correspondingly, the elevated position of the cell is along the azimuth of 135° ("tilt1"). And the magenta line represents the result for $\mathrm{Ra_{max}}$ and the raised position of the cell is along −45° azimuth ("tilt2").

is sensitive to the symmetry of the system. The lack of ideal symmetry in the flow structure is evident even for standing waves, as shown in Figs. 4(c) and 4(d). In the case of the horizontally oriented cell, hot plumes intermittently generate and erupt from the "disturbance regions", establishing a dynamic equilibrium of the azimuthal flow. However, when the cell is tilted by 1° relative to the horizontal plane, and the tilting position needs to be located far away from the regions where plumes naturally burst in horizontal system, the dynamic equilibrium induced by the "thermal disturbances" could be easily disrupted by the effect of tilt. The fluid in the near-tilt-point region, where hot plumes burst, tends to move towards the tilt point due to buoyancy. The competition among different plumes would lead to the fact that the traveling wave moves along a certain direction. Furthermore, the wavy instability caused by tilt generally leads to unstable longitudinal rolls and a disturbance mean flow parallel to the plates which plays as a shear flow, as reported in the study on inclined layer convection [57]. The shear flow can easily turn into circular flow and induce traveling waves in a cylinder RBC system.

Originally, it was planned to perform identical measurements on the traveling wave state SS. However, as the Ra approaches $\mathrm{Ra_{med}}$, the flow state tends to easily transition from a six-roll structure (SS) to a four-roll structure (QS). This transition can be directly observed by analyzing the change in the amplitude series of the second and third Fourier modes of the temperature profiles. Figures 9(a) and 9(b) show the Fourier mode amplitude and phase obtained at $\mathrm{Ra_{min}}$, where the third-order mode dominates throughout the measurement period, and the waves settles in a specific equilibrium position within a small angular range. As Ra increases to $\mathrm{Ra_{med}}$, as shown in Figs. 9(c) and 9(d), the third-order mode gradually gives way to the second-order mode after more than 30 hours, marking the transition from SS to QS. The angular speed of the traveling waves slightly increases posttransition, consistent with independent measurements of QS and SS shown in Fig. 7. At high $\mathrm{Ra_{max}}$, as shown in Figs. 9(e) and 9(f), the mode transition occurs earlier, approximately 6 hours into recording. The time-averaged angular speed after the mode transition is considerably higher than that before the transition. Moreover, the transition seems unidirectional and irreversible, with no reversion from SS to QS observed in our experiments during the 120-hour monitoring period. This flow transition is distinct from the switching back and forth behavior between two metastable states via global bifurcation, which was observed in an annular cell with large geometrical confinement ($\eta = 0.88$) [21]. Therefore, the present study provides additional insights into the dynamical behavior of the annular systems and highlights the importance of studying the mechanisms underlying flow state transitions. Kolodner *et al.* [44] speculated that the transient and spatiotemporal defects that occurred in their experiment appeared to result from the competition between different dynamical states. If this is the case, QS appears to be more stable and competitive than SS in our system.

IV. SUMMARY AND CONCLUSION

We experimentally investigated the flow structures and dynamics of turbulent thermal convection in an annular cell with aspect ratio $\Gamma = 4$ and radius ratio $\eta = 0.5$. The Rayleigh number varies in the range $5.05 \times 10^7 \leqslant \mathrm{Ra} \leqslant 5.05 \times 10^8$, while the Prandtl number is fixed ($\mathrm{Pr} \simeq 5.4$). When the cell is horizontally positioned, both the quadrupole state (QS) and the sextupole state (SS) are stable, forming standing waves. However, when the cell is lifted by 1° from a position significantly deviating from the regions where plumes naturally burst, a traveling wave is observed.

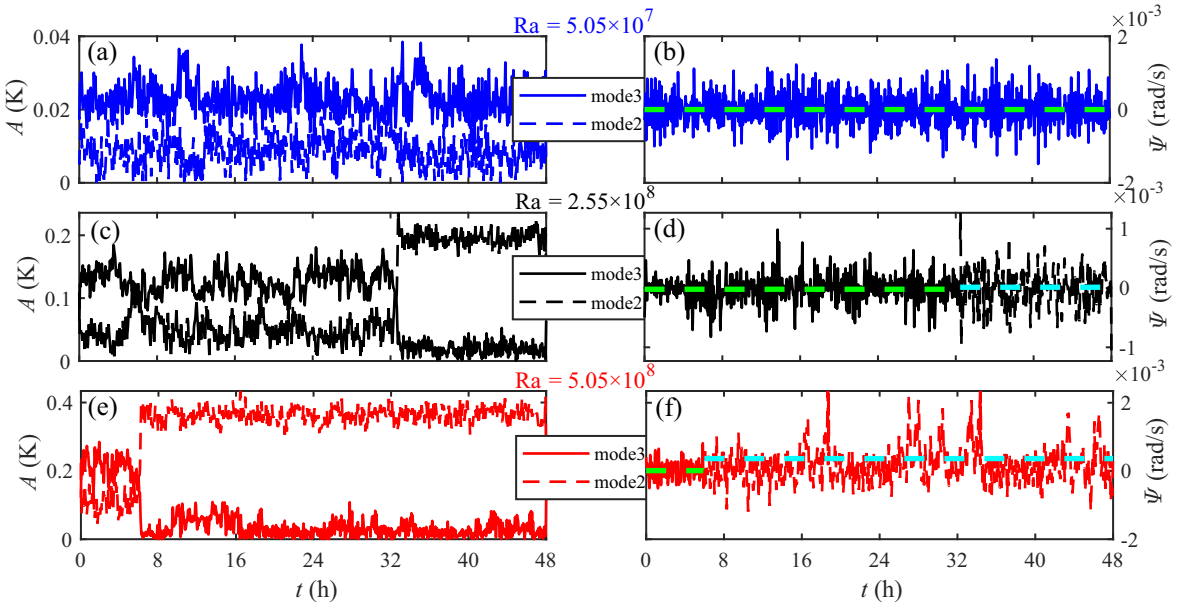

FIG. 9. The time series of the second- and third-order mode amplitudes (left) and traveling-wave angular speed (right) for different Ra during the transition from SS to QS. The third-order mode data are denoted by thin solid lines, while the second-order mode data are indicated by thin dashed lines. The color blue corresponds to $\mathrm{Ra_{min}} = 5.05 \times 10^7$ in (a) and (b), black corresponds to $\mathrm{Ra_{med}} = 2.55 \times 10^8$ in (c) and (d), and red corresponds to $\mathrm{Ra_{max}} = 5.05 \times 10^8$ in (e) and (f). The average values of the angular speed before and after mode switching are shown with thick dashed lines in green and cyan, respectively.

Regarding standing waves, the scaling laws of the Re and Ra are different for the two flow states, QS and SS, with the first having a scaling exponent of 0.56 and the second of only 0.41. With respect to traveling waves, it is found that the movement of the waves is influenced by various factors, such as flow states (or the number of rolls), Ra, and the tilted orientation of the cell. QS travels faster than SS, and higher Ra leads to more stable waves with larger angular speed. Interestingly, SS can evolve into QS during traveling wave motion, but the opposite was not observed in our experiments, suggesting that flow structure evolution may be unidirectional, with QS being more stable. Further research is needed to confirm the existence of this unidirectional behavior of evolution and understand the underlying physical mechanisms.

ACKNOWLEDGMENTS

We benefited from stimulating and helpful discussions with many people, in particular, Q. Zhou, B.-F. Wang, K. L. Chong, J. Shen, J.-K. Zhou, D.-L. Fan, and J.-L. Wu. This work was sponsored by the National Natural Science Foundation of China under Grants No. 12032016, No. 91952102, No. 11972220, and No. 92052201; the Shanghai Science and Technology Program under Project No. 20ZR1419800; and the Shanghai Pujiang Program under Project No. 21PJ1404400.

[1] A. Abdulkadhim, I. M. Abed, and N. Mahjoub Said, Review of natural convection within various shapes of enclosures, Arab. J. Sci. Eng. **46**, 11543 (2021).

[2] A. V. Getling, *Rayleigh-Bénard Convection: Structures and Dynamics*, Vol. 11 (World Scientific, Singapore, 1998).

[3] Y. Zhang, Q. Zhou, and C. Sun, Statistics of kinetic and thermal energy dissipation rates in two-dimensional turbulent Rayleigh-Bénard convection, J. Fluid Mech. **814**, 165 (2017).

[4] Y.-Z. Zhang, C. Sun, Y. Bao, and Q. Zhou, How surface roughness reduces heat transport for small roughness heights in turbulent Rayleigh-Bénard convection, J. Fluid Mech. **836**, R2 (2018).

[5] H. Jiang, X. Zhu, V. Mathai, R. Verzicco, D. Lohse, and C. Sun, Controlling Heat Transport and Flow Structures in Thermal Turbulence Using Ratchet Surfaces, Phys. Rev. Lett. **120**, 044501 (2018).

[6] J.-L. Yang, Y.-Z. Zhang, T.-C. Jin, Y.-H. Dong, B.-F. Wang, and Q. Zhou, The-dependence of the critical roughness height in two-dimensional turbulent Rayleigh–Bénard convection, J. Fluid Mech. **911**, A52 (2021).

[7] D. N. Guzman, Y. Xie, S. Chen, D. F. Rivas, C. Sun, D. Lohse, and G. Ahlers, Heat-flux enhancement by vapour-bubble nucleation in Rayleigh-Bénard turbulence, J. Fluid Mech. **787**, 331 (2016).

[8] K.-Q. Xia, S.-D. Huang, Y.-C. Xie, and L. Zhang, Tuning heat transport via coherent structure manipulation: Recent advances in thermal turbulence, Natl. Sci. Rev. **2023**, nwad012 (2023).

[9] K. L. Chong, S.-D. Huang, M. Kaczorowski, and K.-Q. Xia, Condensation of Coherent Structures in Turbulent Flows, Phys. Rev. Lett. **115**, 264503 (2015).

[10] K. L. Chong and K. Q. Xia, Exploring the severely confined regime in Rayleigh-Bénard convection, J. Fluid Mech. **805**, R4 (2016).

[11] S. Liu, L. Jiang, K.-L. Chong, X. Zhu, Z.-H. Wan, R. Verzicco, R. J. Stevens, D. Lohse, and C. Sun, From Rayleigh-Bénard convection to porous-media convection: How porosity affects heat transfer and flow structure, J. Fluid Mech. **895**, A18 (2020).

[12] B.-F. Wang, Q. Zhou, and C. Sun, Vibration-induced boundary-layer destabilization achieves massive heat-transport enhancement, Sci. Adv. **6**, eaaz8239 (2020).

[13] H. Jiang, X. Zhu, D. Wang, S. G. Huisman, and C. Sun, Supergravitational turbulent thermal convection, Sci. Adv. **6**, eabb8676 (2020).

[14] J.-Z. Wu, Y.-H. Dong, B.-F. Wang, and Q. Zhou, Phase decomposition analysis on oscillatory Rayleigh–Bénard turbulence, Phys. Fluids **33**, 045108 (2021).

[15] X.-Q. Guo, B.-F. Wang, J.-Z. Wu, K. L. Chong, and Q. Zhou, Turbulent vertical convection under vertical vibration, Phys. Fluids **34**, 055106 (2022).

[16] K.-L. Chong, Y. Yang, S.-D. Huang, J.-Q. Zhong, R. J. Stevens, R. Verzicco, D. Lohse, and K.-Q. Xia, Confined Rayleigh-Bénard, Rotating Rayleigh-Bénard, and Double Diffusive Convection: A Unifying View on Turbulent Transport Enhancement through Coherent Structure Manipulation, Phys. Rev. Lett. **119**, 064501 (2017).

[17] Z. Wang, V. Mathai, and C. Sun, Self-sustained biphasic catalytic particle turbulence, Nat. Commun. **10**, 3333 (2019).

[18] R. Yang, K. L. Chong, Q. Wang, R. Verzicco, O. Shishkina, and D. Lohse, Periodically Modulated Thermal Convection, Phys. Rev. Lett. **125**, 154502 (2020).

[19] C.-B. Zhao, Y.-Z. Zhang, B.-F. Wang, J.-Z. Wu, K. L. Chong, and Q. Zhou, Modulation of turbulent Rayleigh-Bénard convection under spatially harmonic heating, Phys. Rev. E **105**, 055107 (2022).

[20] C.-B. Zhao, B.-F. Wang, J.-Z. Wu, K. L. Chong, and Q. Zhou, Suppression of flow reversals via manipulating corner rolls in plane Rayleigh–Bénard convection, J. Fluid Mech. **946**, A44 (2022).

[21] Y.-C. Xie, G.-Y. Ding, and K.-Q. Xia, Flow Topology Transition via Global Bifurcation in Thermally Driven Turbulence, Phys. Rev. Lett. **120**, 214501 (2018).

[22] G. A. Glatzmaiers and P. H. Roberts, A three-dimensional self-consistent computer simulation of a geomagnetic field reversal, Nature (London) **377**, 203 (1995).

[23] J. Marshall and F. Schott, Open-ocean convection: Observations, theory, and models, Rev. Geophys. **37**, 1 (1999).

[24] M. Krishnan, V. M. Ugaz, and M. A. Burns, PCR in a Rayleigh-Bénard convection cell, Science **298**, 793 (2002).

[25] M. Elmo and O. Cioni, Low mach number model for compressible flows and application to HTR, Nucl. Eng. Des. **222**, 117 (2003).

[26] C.-T. Sun and D.-F. Xue, Pulling growth technique towards rare earth single crystals, Sci. China Technol. Sci. **61**, 1295 (2018).

[27] C. Sun and Q. Zhou, Experimental techniques for turbulent Taylor–Couette flow and Rayleigh-Bénard convection, Nonlinearity **27**, R89 (2014).

[28] H. J. Brauckmann, B. Eckhardt, and J. Schumacher, Heat transport in Rayleigh-Bénard convection and angular momentum transport in Taylor–Couette flow: A comparative study, Phil. Trans. R. Soc. A. **375**, 20160079 (2017).

[29] J. S. Yoo, M. U. Kim, and D. H. Choi, Convective instability of a fluid layer confined in a vertical annulus heated from below, Int. J. Heat Mass Transf. **31**, 2285 (1988).

[30] B.-F. Wang, Z.-W. Guo, D.-J. Ma, and D.-J. Sun, Instabilities and pattern evolution in a vertically heated annulus, Sci. China Phys. Mech. Astron. **56**, 257 (2013).

[31] B.-F. Wang, Z.-H. Wan, D.-J. Ma, and D.-J. Sun, Rayleigh-Bénard convection in a vertical annular container near the convection threshold, Phys. Rev. E **89**, 043014 (2014).

[32] X. Zhu, L.-F. Jiang, Q. Zhou, and C. Sun, Turbulent Rayleigh-Bénard convection in an annular cell, J. Fluid Mech. **869**, R5 (2019).

[33] X. Zhu and Q. Zhou, Flow structures of turbulent Rayleigh-Bénard convection in annular cells with aspect ratio one and larger, Acta Mech. Sin. **37**, 1291 (2021).

[34] D. Wang, H. Jiang, S. Liu, X. Zhu, and C. Sun, Effects of radius ratio on annular centrifugal Rayleigh-Bénard convection, J. Fluid Mech. **930**, A19 (2022).

[35] H.-D. Xi and K.-Q. Xia, Flow mode transitions in turbulent thermal convection, Phys. Fluids **20**, 055104 (2008).

[36] S. Weiss and G. Ahlers, Turbulent Rayleigh-Bénard convection in a cylindrical container with aspect ratio $\gamma = 0.50$ and Prandtl number $pr = 4.38$, J. Fluid Mech. **676**, 5 (2011).

[37] H.-D. Xi, Y.-B. Zhang, J.-T. Hao, and K.-Q. Xia, Higher-order flow modes in turbulent Rayleigh-Bénard convection, J. Fluid Mech. **805**, 31 (2016).

[38] G. M. Horstmann, D. Schiepel, and C. Wagner, Experimental study of the global flow-state transformation in a rectangular Rayleigh-Bénard sample, Int. J. Heat Mass Transf. **126**, 1333 (2018).

[39] Q. Wang, R. Verzicco, D. Lohse, and O. Shishkina, Multiple States in Turbulent Large-Aspect-Ratio Thermal Convection: What Determines the Number of Convection Rolls? Phys. Rev. Lett. **125**, 074501 (2020).

[40] L. Zwirner, A. Tilgner, and O. Shishkina, Elliptical Instability and Multiple-Roll Flow Modes of the Large-Scale Circulation in Confined Turbulent Rayleigh-Bénard Convection, Phys. Rev. Lett. **125**, 054502 (2020).

[41] K. Borońska and L. S. Tuckerman, Standing and travelling waves in cylindrical Rayleigh-Bénard convection, J. Fluid Mech. **559**, 279 (2006).

[42] M. Wanschura, H. C. Kuhlmann, and H. J. Rath, Three-dimensional instability of axisymmetric buoyant convection in cylinders heated from below, J. Fluid Mech. **326**, 399 (1996).

[43] B. Hof, P. G. J. Lucas, and T. Mullin, Flow state multiplicity in convection, Phys. Fluids **11**, 2815 (1999).

[44] P. Kolodner, D. Bensimon, and C. M. Surko, Traveling-wave Convection in an Annulus, Phys. Rev. Lett. **60**, 1723 (1988).

[45] R. J. Adrian, Particle-imaging techniques for experimental fluid mechanics, Annu. Rev. Fluid Mech. **23**, 261 (1991).

[46] K.-Q. Xia, C. Sun, and S.-Q. Zhou, Particle image velocimetry measurement of the velocity field in turbulent thermal convection, Phys. Rev. E **68**, 066303 (2003).

[47] C. Sun, K.-Q. Xia, and P. Tong, Three-dimensional flow structures and dynamics of turbulent thermal convection in a cylindrical cell, Phys. Rev. E **72**, 026302 (2005).

[48] Y.-Z. Li, X. Chen, A. Xu, and H.-D. Xi, Counter-flow orbiting of the vortex centre in turbulent thermal convection, J. Fluid Mech. **935**, A19 (2022).

[49] P. Chorin, F. Moreau, and D. Saury, Heat transfer modification induced by a localized thermal disturbance in a differentially-heated cavity, Int. J. Therm. Sci. **125**, 101 (2018).

[50] K. L. Chong, G. Ding, and K.-Q. Xia, Multiple-resolution scheme in finite-volume code for active or passive scalar turbulence, J. Comput. Phys. **375**, 1045 (2018).

[51] S. Lam, X.-D. Shang, S.-Q. Zhou, and K.-Q. Xia, Prandtl number dependence of the viscous boundary layer and the Reynolds numbers in Rayleigh-Bénard convection, Phys. Rev. E **65**, 066306 (2002).

[52] X. Chen, S.-D. Huang, K.-Q. Xia, and H.-D. Xi, Emergence of substructures inside the large-scale circulation induces transition in flow reversals in turbulent thermal convection, J. Fluid Mech. **877**, R1 (2019).

[53] S. Grossmann and D. Lohse, Prandtl and Rayleigh number dependence of the Reynolds number in turbulent thermal convection, Phys. Rev. E **66**, 016305 (2002).

[54] E. Brown and G. Ahlers, The origin of oscillations of the large-scale circulation of turbulent Rayleigh-Bénard convection, J. Fluid Mech. **638**, 383 (2009).

[55] K. L. Chong, J.-Q. Shi, G.-Y. Ding, S.-S. Ding, H.-Y. Lu, J.-Q. Zhong, and K.-Q. Xia, Vortices as Brownian particles in turbulent flows, Sci. Adv. **6**, eaaz1110 (2020).

[56] S. Guo, S. Zhou, X. Cen, L. Qu, Y. Lu, L. Sun, and X. Shang, The effect of cell tilting on turbulent thermal convection in a rectangular cell, J. Fluid Mech. **762**, 273 (2015).

[57] F. H. Busse and R. M. Clever, Three-dimensional convection in an inclined layer heated from below, J. Eng. Math. **26**, 1 (1992).